

Entropy based flux limiting scheme for conservation laws

Georgios Doulis^{1,2}, Sebastiano Bernuzzi², and Wolfgang Tichy³

¹*Institut für Theoretische Physik, Goethe-Universität Frankfurt, 60438 Frankfurt am Main*

²*Theoretisch-Physikalisches Institut, Friedrich-Schiller-Universität Jena, 07743 Jena and*

³*Department of Physics, Florida Atlantic University, Boca Raton, FL 33431*

(Dated: January 11, 2024)

The construction of high-resolution shock-capturing schemes is vital in producing highly accurate gravitational waveforms from neutron star binaries. The entropy based flux limiting (EFL) scheme is able to perform fast converging binary neutron star merger simulations reaching up to fourth-order convergence in the gravitational waveform phase. Here, we extend the applicability of the EFL method beyond special/general relativistic hydrodynamics to scalar conservation laws and show how to treat systems without a thermodynamic entropy. This is an indication that the method has universal applicability to any system of partial differential equations that can be written in conservation form. We also present some further very challenging special/general relativistic hydrodynamics applications of the EFL method and use it to construct eccentricity reduced initial data for a specific neutron star binary and show up to optimal fifth-order convergence in the gravitational waveform phase for this simulation.

I. INTRODUCTION

Binary neutron star (BNS) coalescences are one of the confirmed [1, 2] sources of gravitational waves (GW) detected by the LIGO-VIRGO interferometers. Numerical relativity (NR) is able to produce merger waveforms that replicate these GWs accurately enough for BNS parameter estimation. The production of highly accurate numerical waveforms plays a vital role in understanding the properties of neutron star (NS) binaries during the inspiral, merger and postmerger regime. In this spirit, several high-resolution shock-capturing (HRSC) schemes [3] have been developed over the years aiming in increasing the accuracy and the convergence properties of the numerically produced waveforms. Going beyond second-order convergence is currently the major challenge for the existing HRSC schemes, which has been pointed out long ago, but addressed only in a few places [4–7]. Here, we focus on a specific family of flux altering HRSC methods: the flux-limiters [8], which have been proven very successful in dealing with shocks and suppressing spurious oscillations.

In [9] a fast converging HRSC scheme that utilises the local entropy production in the design of an entropy based flux-limiter (EFL) was proposed. The EFL scheme developed from an entropy method that started as an artificial viscosity method [10, 11] and grew with time to a flux-limiting scheme [12]. In [12], for the first time, entropy was used in the design of a flux-limiter. The EFL scheme, apart from overcoming the shortcomings of the method developed in [12], is considerably more automated and simpler in its implementation. These features make the EFL method universally applicable to different special and general relativistic scenarios. The EFL scheme was successfully used in [9] to evolve several different BNS systems and managed to deliver up to fourth-order convergent waveforms in the dominant (2, 2)-mode and in the subdominant (3, 2)- and (4, 4)-mode.

In the present work we extend the applicability of the

EFL method to scalar conservation laws without a thermodynamically defined entropy. To do so, an auxiliary entropy functional has to be defined [11], which can be used to flag the presence of non-smooth features in the solution space. This entropy can be used, like in [9], to define the local weights entering the usual definition of the entropy flux-limiter. The weights combine an unfiltered high-order flux used in regions of smooth flow with a stable low- or high-order flux used in regions of non-smooth flow.

We also use the EFL method for the first time in the construction of BNS initial data. (Notice that now we have a well defined thermodynamic entropy, therefore the use of the well established EFL machinery of [9] is more than sufficient.) In [9], the EFL scheme was exclusively used for the temporal evolution of initial data computed with the Lorene library [13]. Here, we involve the EFL method in the construction of eccentricity reduced initial data with the SGRID code [14] and study the effect of this action on the accuracy and the convergence properties of the produced merger waveforms.

The article is structured as follows. Theoretical and numerical aspects of the EFL method are discussed in Sec. II and the details of its numerical implementation in Sec. III. The first application of the EFL method to scalar conservation laws is presented in Sec. IV. Sec. V includes our results for some standard benchmark tests of special relativity and in Sec. VI the performance of our method is tested against three-dimensional general relativistic non-static/stationary single NS configurations. Sec. VII contains our results of the first BNS simulation where the EFL method is not only used for the temporal evolution, but also in the construction of the initial data. Finally, we conclude in Sec. VIII.

Throughout this work we use geometric units. We set $c = G = 1$ and the masses are expressed in terms of solar masses M_{\odot} .

II. EFL METHOD

In the present work, the entropy flux limiting scheme developed in [9] is extended to systems without a thermodynamically defined entropy. Therefore, here, we consider any system of PDEs that can be written in conservation form:

$$\partial_t \mathbf{Q} + \partial_i \mathbf{F}^i(\mathbf{Q}) = \mathbf{S}, \quad (1)$$

where the summation is performed over the spatial dimensions, \mathbf{Q} is the vector of the conserved variables, \mathbf{F}^i the vector of the physical fluxes, and \mathbf{S} is the vector of the sources. From the plethora of system that can be written in the form (1), in the following, we are going to study the scalar transport and Burgers equations and the equations of special and general relativistic hydrodynamics [15].

The basic idea of the EFL method consists of expressing the numerical fluxes resulting from the spatial discretisation of (1) as a superposition of an unstable high-order and a stable low- or high-order flux, where the weight dictating the transition between the two fluxes is computed from the local entropy production of the system under investigation. Thus, the entropy of the system is used as a ‘‘shock detector’’ indicating when to switch from the unstable high-order scheme to the stable one.

For systems with thermodynamic entropy the implementation of the EFL method follows the exposition in [9]. In the following, we will show how to extend the EFL machinery of [9] to systems without a physically motivated definition of entropy, like the ones of Sec. IV.

In accordance with [9], we start by approximating the spatial derivative of the x component, \mathbf{F}^x , of the physical flux appearing in (1) with the conservative finite-difference formula¹

$$\partial_x F_i^x = \frac{\hat{f}_{i+1/2} - \hat{f}_{i-1/2}}{h}, \quad (2)$$

where F^x is any one of the components of \mathbf{F}^x with $F_i^x = F^x(x_i)$, $\hat{f}_{i\pm 1/2}$ are the numerical fluxes at the cell interfaces and h is the spatial grid spacing.

In order to construct a flux-limiter, the numerical fluxes in (2) have to be split into two contributions in the usual way [3]:

$$\hat{f}_{i\pm 1/2} = \theta_{i\pm 1/2} \hat{f}_{i\pm 1/2}^{\text{HO}} + (1 - \theta_{i\pm 1/2}) \hat{f}_{i\pm 1/2}^{\text{LO}}. \quad (3)$$

The quantities entering the r.h.s of (3) read:

- f^{HO} is a high-order (HO) unstable numerical flux used in regions where the numerical solution is smooth.

- f^{LO} is a high- or low-order (LO) stable numerical flux used in regions where the numerical solution develops non-smooth features. Notice that in order to be consistent with previous work [9, 12], we keep the notation LO although in the following we use exclusively a stable high-order scheme to approximate f^{LO} .

- $\theta \in [0, 1]$ is a continuous weight function indicating how much from the numerical fluxes f^{HO} and f^{LO} to use at every instance.

In particular, the flux \hat{f}^{HO} is built using the Rusanov Lax-Friedrichs flux-splitting technique and performing the reconstruction on the characteristic fields [7, 16]. A fifth-order central unfiltered stencil (CS5) is always used for reconstruction. The flux \hat{f}^{LO} is approximated by the LLF central scheme with reconstruction performed on the primitive variables [17]. Primitive reconstruction here is performed with the fifth-order weighted-essentially-non-oscillatory finite difference schemes WENO5 [18] and WENOZ [19].² With this choice, originally introduced in [9], we generalise the traditional notion of a flux-limiter where \hat{f}^{LO} is always a LO monotone flux [3, 22].

The weight function θ is computed from the so-called *entropy production function* ν , a quantity that depends on the local entropy production. Explicitly, the relation between θ and ν is

$$\theta_{i\pm 1/2} = 1 - \frac{1}{2}(\nu_i + \nu_{i\pm 1}). \quad (4)$$

Below, we summarise how to compute ν for systems with and without thermodynamically defined entropy.

Systems with thermodynamic entropy: In order to quantify the relation between ν and the entropy produced by the systems of Secs. V, VI, and VII, we define the specific entropy (entropy per unit mass) of any piecewise polytropic EoS³ as

$$s = \ln \left(\frac{p}{\rho^\Gamma} \right), \quad (5)$$

where the pressure is computed in accordance with the EoS in use.

Following [12], we employ the second law of thermodynamics to define the entropy residual:

$$\mathcal{R} = \nabla_\mu (s \rho u^\mu) \geq 0, \quad (6)$$

which provides a quantitative estimation of the rate of the entropy produced by the system under study. Using

¹ For clarity and without loss of generality, from now on the presentation is restricted to one dimension, say x . A multidimensional scheme is obtained by considering fluxes in each direction separately and adding them to the r.h.s.

² To produce the results of FIG. 5 the third-order convex-essentially-non-oscillatory (CENO3) algorithm [20, 21] is used to perform primitive reconstruction.

³ For a more general EoS the specific entropy s can be taken from the EoS.

the continuity equation and writing the 4-velocity u^μ in terms of the fluid 3-velocity v^i , the above expression can be written [12] in terms of the time and spatial derivatives of the specific entropy as

$$\mathcal{R} = \frac{\rho W}{\alpha} (\partial_t s + (\alpha v^i - \beta^i) \partial_i s). \quad (7)$$

Following the argumentation in [9], we suppress the multiplication factor $\frac{\rho W}{\alpha}$ and replace \mathcal{R} by

$$R = \partial_t s + (\alpha v^i - \beta^i) \partial_i s, \quad (8)$$

which amounts to a rescaling of \mathcal{R} so that the coefficient of $\partial_t s$ is equal to one.

Systems without thermodynamic entropy: The systems of Sec. IV do not have an EoS which can be used to define the entropy. For such systems (1) takes the scalar form

$$\partial_t Q + \partial_i F^i(Q) = S. \quad (9)$$

Following [10, 11], we define an entropy for (9) by introducing the so-called entropy pair: $E(Q)$ and $\mathcal{F}^i(Q)$. The convex function E is called entropy functional and $\mathcal{F}^i(Q)$ is the associated entropy flux given by the expression

$$\mathcal{F}^i(Q) = \int \partial_Q E(Q) \partial_Q F^i(Q) dQ. \quad (10)$$

The entropy pair can be used to define an entropy residual:

$$R = \partial_t E(Q) + \partial_i \mathcal{F}^i(Q). \quad (11)$$

For convex physical fluxes F^i , like the ones of Sec. IV, the entropy pair generated by the choice $E(Q) = \frac{1}{2}Q^2$ has been proven [10, 11] enough for our purposes here. With the above choice of the entropy functional, the entropy residual (11) can be straightforwardly computed for the systems of Sec. IV.

Finally, we define the so-called *entropy production function*, for systems with and without thermodynamic entropy, in terms of the rescaled entropy residual R defined by (8) or (11),

$$\nu_E = c_E |R|, \quad (12)$$

where c_E is a tunable constant used to scale the absolute value of R . In all our three-dimensional general relativistic simulations of Secs. VI and VII we do not have to tune c_E , its value is set always to unity, i.e. $c_E = 1$. For the one-dimensional simulations of Secs. IV and V the tunable constant c_E is set either to 10 or 50 depending on the case studied.

Keeping in mind that the parameter θ cannot exceed unity, we have to impose a maximum value of $\nu_{\max} = 1$ for the entropy production function in order to ensure that the rhs of (4) does not exceed the range $[0, 1]$. Accordingly, the entropy production function entering (4) is given by

$$\nu = \min[\nu_E, 1]. \quad (13)$$

III. NUMERICAL IMPLEMENTATION

The finite differencing code BAM [7, 17, 23, 24] is used to solve numerically the system of equations of the form (1) discussed in the present work. The aforementioned EFL method is implemented into BAM and is part of its infrastructure. BAM uses the method-of-lines with Runge-Kutta (RK) time integration and finite differences for the approximation of spatial derivatives. The value of the Courant-Friedrich-Lewy (CFL) condition is set to 0.25 for all runs.

For the numerical implementation of the EFL method the BAM routines computing the numerical fluxes had to be modified in order to accommodate the hybrid flux (3). In order to compute the entropy production function we have to approximate the time and spatial derivatives of the entropy quantities in (8) and (11). We use finite differences to do so. Specifically, the spatial derivatives are approximated with a standard centered finite-difference stencil of order $p + 1$ or higher, where p is the order of the stencil used to approximate the physical fluxes. (In the present work we use $p = 5$.) With this restriction it is ensured that the entropy production function ν converges to zero in the smooth regions faster than the overall convergence of the scheme. The time derivative is also approximated with finite differences. We employ a third-order one-sided stencil by using, at every Runge-Kutta iteration, the current value of the specific entropy and the values at the three previous timesteps. The fact that we manage to achieve higher than third-order convergence in the majority of our simulations can be possibly attributed to the dominance of the spatial error over the time discretization error.

The numerical domain contains a mesh made of a hierarchy of cell-centered nested Cartesian boxes and consists of L refinement levels $l = 0, \dots, L - 1$ ordered with increasing resolution. Each refinement level is made out of one or more equally spaced Cartesian grids with grid spacing h_l . There are n points per direction on each grid plus a certain number of buffer points on each side. (For simplicity, we always quote grid sizes without buffer points.) The resolution between two consecutive levels is doubled such that the grid spacing at level l is $h_l = h_0/2^l$, where h_0 is the grid spacing of the coarsest level. The inner levels move in accordance with the moving boxes technique, while the outer levels remain fixed. The number of points in one direction of a moving level can be set to a different value than the number of points of a fixed level. The coordinate extent of a grid at level l entirely contains grids at any level greater than l . The moving refinement levels always stay within the coarsest level. For the time evolution of the grid the Berger-Oliger algorithm is employed enforcing mass conservation across refinement boundaries [24, 25]. Restriction and prolongation is performed for the matter fields with a fourth-order WENO scheme and for the metric fields with a sixth-order Lagrangian scheme. Interpolation in Berger-Oliger time stepping is performed at second-order.

The derivatives of the metric components are approximated by fourth-order accurate finite-differencing stencils. In addition, sixth-order artificial dissipation operators are employed to stabilize noise from mesh refinement boundaries. The general relativistic hydrodynamic equations (1) are solved by means of a high-resolution-shock-capturing method [17] based on primitive reconstruction and the aforementioned high-order entropy limited scheme for the numerical fluxes. In the present work spacetime is dynamically evolved using either the BSSNOK [26–28] or the Z4c [29, 30] evolution scheme.

Vacuum regions are simulated with the introduction of a static, low-density, cold atmosphere in the vacuum region surrounding the star [17]. The atmosphere density is defined as

$$\rho_{\text{atm}} = f_{\text{atm}} \max \rho(t=0). \quad (14)$$

All grid points with rest-mass density below a threshold value $\rho_{\text{thr}} = f_{\text{thr}} \rho_{\text{atm}}$ are set automatically to ρ_{atm} . Transition to low-density regions is one of the main sources of error in NS simulations. This is a common feature in all current numerical relativity implementations of NS dynamics. To deal with this challenging feature they also make use of similar assumptions and algorithms at low densities as those employed here.

The equations of state (EoS) used in the present work are the following. For the special relativistic tests of Sec. V we use a Γ -law EoS,

$$p = (\Gamma - 1)\rho\epsilon, \quad (15)$$

with Γ the adiabatic index. The neutron star matter of the single neutron star evolutions of Sec. VI is also modelled by a Γ -law EoS of the form (15). Finally, the matter of the neutron stars comprising the binary of Sec. VII is described by a SLy EoS [31]. The latter is implemented by a piecewise polytrope fit [32], and thermal effects are modeled by an additive pressure contribution given by the Γ -law EoS with $\Gamma = 1.75$ [17, 33, 34].

IV. SCALAR 1D TESTS

A. Transport equation with non-smooth initial data

We start from the simplest one-dimensional scalar equation that describes the evolution of shocks:

$$\partial_t u(t, x) + \partial_x u(t, x) = 0 \quad \text{with} \quad u(0, x) = u_0(x). \quad (16)$$

In order to test the convergence properties of the EFL method we start with smooth initial data of the form $u_0(x) = e^{-40x^2}$. The exact solution is infinitely smooth and is deduced from the initial data: $u(t, x) = u_0(x - t)$. Convergence studies are performed on an equidistant grid with range $[-1, 1]$ that is progressively refined with $n = 2^k \times 200$ grid points, where $k = 0, \dots, 5$. Different

high-order RKp (with $3 \leq p \leq 5$) schemes are used for the temporal evolution. Our convergence analysis indicates that optimal convergences p is achieved in all cases independently of the scheme used for the LO flux.

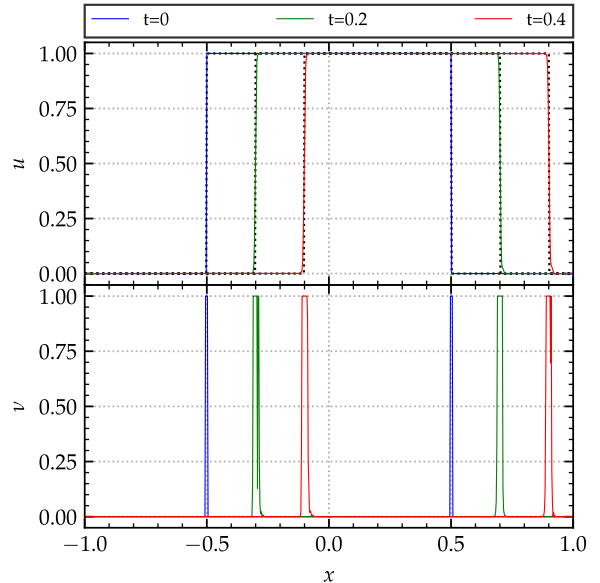


FIG. 1. Transport equation with non-smooth square wave initial data. The numerical solution (top panel) and the corresponding entropy production profile (bottom panel) are depicted at different stages of the evolution. The solution is computed with the WENOZ reconstruction scheme on a grid of 800 points with resolution $\Delta x = 2.5 \times 10^{-3}$. Dotted black lines depict the exact solution.

Next, we consider non-smooth square wave initial data:

$$u_0(x) = \begin{cases} 1, & \text{if } -0.5 \leq x \leq 0.5, \\ 0, & \text{otherwise.} \end{cases} \quad (17)$$

The grid set-up is the same as above. The initial data (17) is evolved with a RK4 routine and the CFL condition is set to 0.125. The WENOZ scheme is used for the LO flux and the value of the tunable constant is set to $c_E = 10$. FIG. 1 depicts the numerical solution u of (16) and the corresponding entropy production profile ν at different stages of the evolution on a grid composed by 800 grid-points ($\Delta x = 2.5 \times 10^{-3}$). It is apparent that the EFL method locates successfully the position of the shocks and tracks them efficiently during the evolution. The fact that around the shocks of the square wave $\nu = 1$ guarantees the use of the non-oscillatory LO flux there. Thus, the EFL method is able to suppress the emergence of oscillations around the vicinity of the shocks while achieving HO convergence on the rest of the computational domain where the solution is smooth. In addition, the behaviour of the entropy production profiles presented in FIG. 2 entails that with increasing resolution the entropy production gets better localised around

the shocks and thus reduces the impact of the LO flux only to areas very close to the shocks.

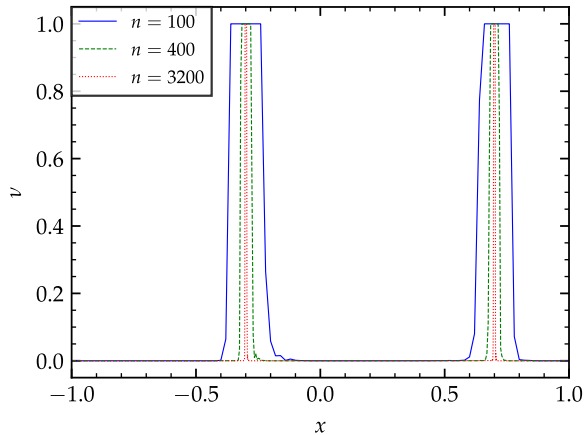


FIG. 2. Entropy production profiles for the transport equation with increasing resolution. The profile of ν at $t = 0.2$ for a low $n = 100$ (solid blue line), an intermediate $n = 400$ (dashed green line) and a high $n = 3200$ (dotted red line) resolution. The solution is computed with the WENOZ reconstruction scheme.

Finally, TABLE I contains the results of the convergence analysis for the numerical solution of FIG. 1 at $t = 0.2$. The observed convergence rates are in accordance with their theoretically expected values [3] of 1 and 0.5 for the norms L_1 and L_2 , respectively. During the evolution the convergence rates are kept constant. Using lower than fifth order reconstruction schemes for the LO flux results in slightly smaller convergence rates, something expected as the lower accuracy of the LO flux drives down the overall accuracy of the entropy flux limiter. The use of other RK time integration routines, like RK3 and RK5, did not significantly affect the results of TABLE I.

TABLE I. Convergence analysis of the numerical solution of FIG. 1 at $t = 0.2$. L_1 and L_2 are normalised norms and the convergence rate is calculated as the \log_2 of the ratio of two successive normalised norms.

n	L_1	Conv.	L_2	Conv.
200	8.8×10^{-3}	–	4.8×10^{-2}	–
400	5.1×10^{-3}	0.802	3.7×10^{-2}	0.398
800	2.9×10^{-3}	0.802	2.8×10^{-2}	0.396
1600	1.7×10^{-3}	0.821	2.1×10^{-2}	0.397
3200	9.3×10^{-4}	0.834	1.6×10^{-2}	0.401
6400	5.2×10^{-4}	0.836	1.2×10^{-2}	0.412

B. Burgers equation

Next, we consider the inviscid Burgers equation in one-dimension:

$$\partial_t u(t, x) + u(t, x) \partial_x u(t, x) = 0 \quad \text{with} \quad u(0, x) = u_0(x).$$

This is the simplest non-linear scalar equation that develops shocks from originally smooth initial data:

$$u_0(x) = e^{-40x^2}. \quad (18)$$

During the evolution the smooth initial profile becomes steeper and steeper and at around $t \simeq 0.1843$ a shock is formed.

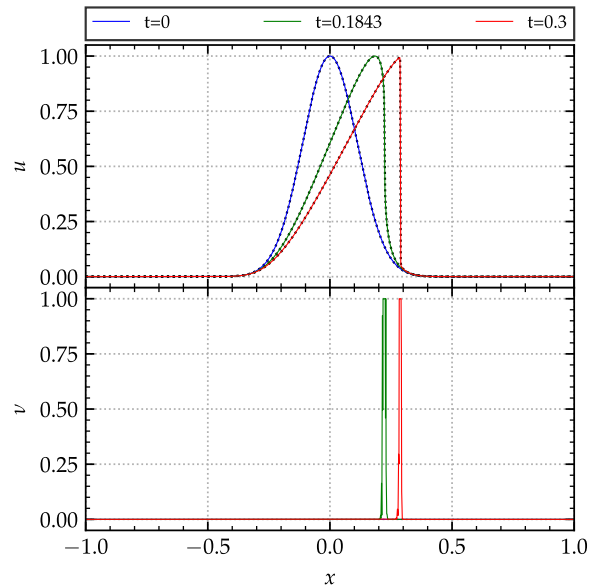


FIG. 3. Burgers equation. The numerical solution (top panel) and the corresponding entropy production profile (bottom panel) are depicted at different stages of the evolution. The solution is computed with the WENOZ reconstruction scheme on a grid of 1600 points with resolution $\Delta x = 1.25 \times 10^{-3}$. Dotted black lines depict the exact solution.

The exact solution is derived from the initial data (18) in the implicit form $u(t, x) = u_0(x - ut)$. The grid setup is the same as in the case of the transport equation, see Sec. IV A. An RK4 routine is used for the temporal evolution and the CFL condition is set to 0.125. The WENOZ scheme is used for the LO flux and the value of the tunable constant is set to $c_E = 10$. FIG. 3 depicts the numerical solution of Burgers equation (top panel) for the initial data (18) and the corresponding entropy production profile (bottom panel) at different stages of the evolution on a grid of 1600 grid-points ($\Delta x = 1.25 \times 10^{-3}$). It is evident that the EFL method recognizes when the solution is smooth—the entropy production is zero—and, in addition, locates successfully the position of the emerging shock and tracks it efficiently during the

evolution. It can be also confirmed by inspection that the EFL solutions are oscillation-free. The localisation of the entropy production profiles with increasing resolution first observed in FIG. 2 is also observed here.

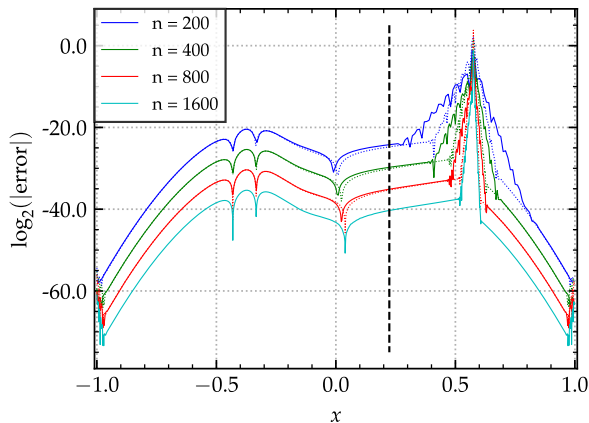


FIG. 4. Convergence to zero with increasing resolution of the error between the numerical and the exact solution of Burgers equation at $t = 1$. The vertical dashed black line depicts the position at which the shock is first formed. Dotted lines show results scaled to fifth-order.

FIG. 4 depicts the numerical error with increasing resolution over the whole computational domain at $t = 1$. Optimal fifth-order convergence is observed at the parts of the domain where the solution is smooth—dotted lines show results scaled to fifth-order. As expected close to the location of the shock the convergence drops to first-order. The position of the right-moving shock can be easily identified by the lower order convergence spike at $x \approx 0.6$. It is clear that the movement of the shock through the computational grid does not contaminate the rest of the numerical domain with its low order convergence. It is evident that the points of the computational domain affected by the shock recover the optimal fifth-order convergence almost instantly. Therefore, lower convergence is a local characteristic of our solution confined to the neighborhood of the shock.

In FIG. 5 the convergence rates with respect to the L_1 -norm for the numerical solution of Burgers equation are computed at different stages of the evolution for two different choices of the LO flux. At early stages of the evolution the convergence rates maintain their optimal high-order values. When the shock starts forming—see vertical dashed black line—the rates decrease rapidly and, after the shock has been fully formed, reach a plateau at around 1. Notice that in the smooth region before the formation of the shock, the use of a lower than fifth-order reconstruction scheme, i.e. CENO3, leads to slightly smaller convergence rates. The use of other RK routines does not alter the convergence rates of FIG. 5 significantly.

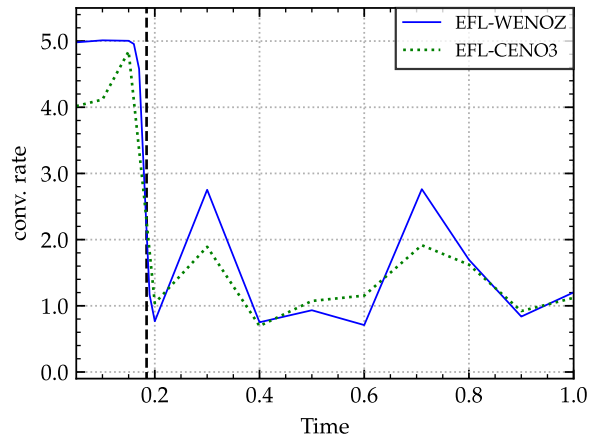


FIG. 5. Convergence rates with respect to the L_1 -norm for the numerical solution of Burgers equation. The behaviour of the convergence rates with time for two different LO schemes is shown: EFL-WENOZ (solid blue line) and EFL-CENO3 (dotted green line). The vertical dashed black line depicts the instant at which the shock is first formed.

V. SPECIAL RELATIVISTIC 1D TESTS

A. Simple wave

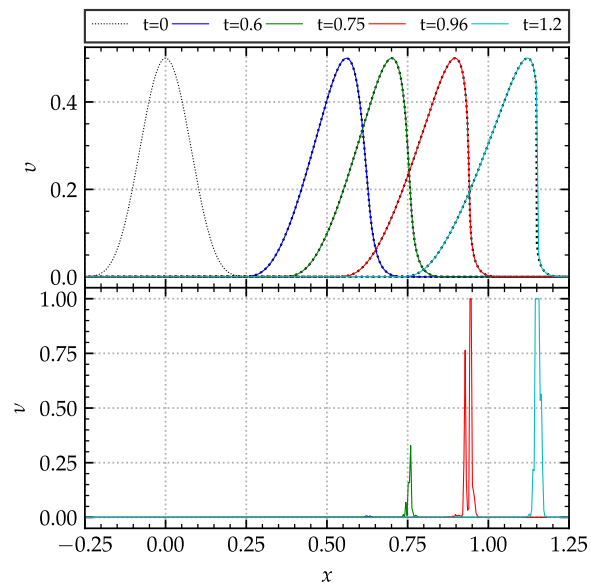


FIG. 6. Simple wave. The numerical solution of the velocity (top panel) and the corresponding entropy production profile (bottom panel) are depicted at different stages of the evolution. The solution is computed with the WENOZ reconstruction scheme on a grid of 1600 points with resolution $\Delta x = 1.875 \times 10^{-3}$. Dotted black lines depict the exact solution.

Relativistic simple waves are exact analytical solu-

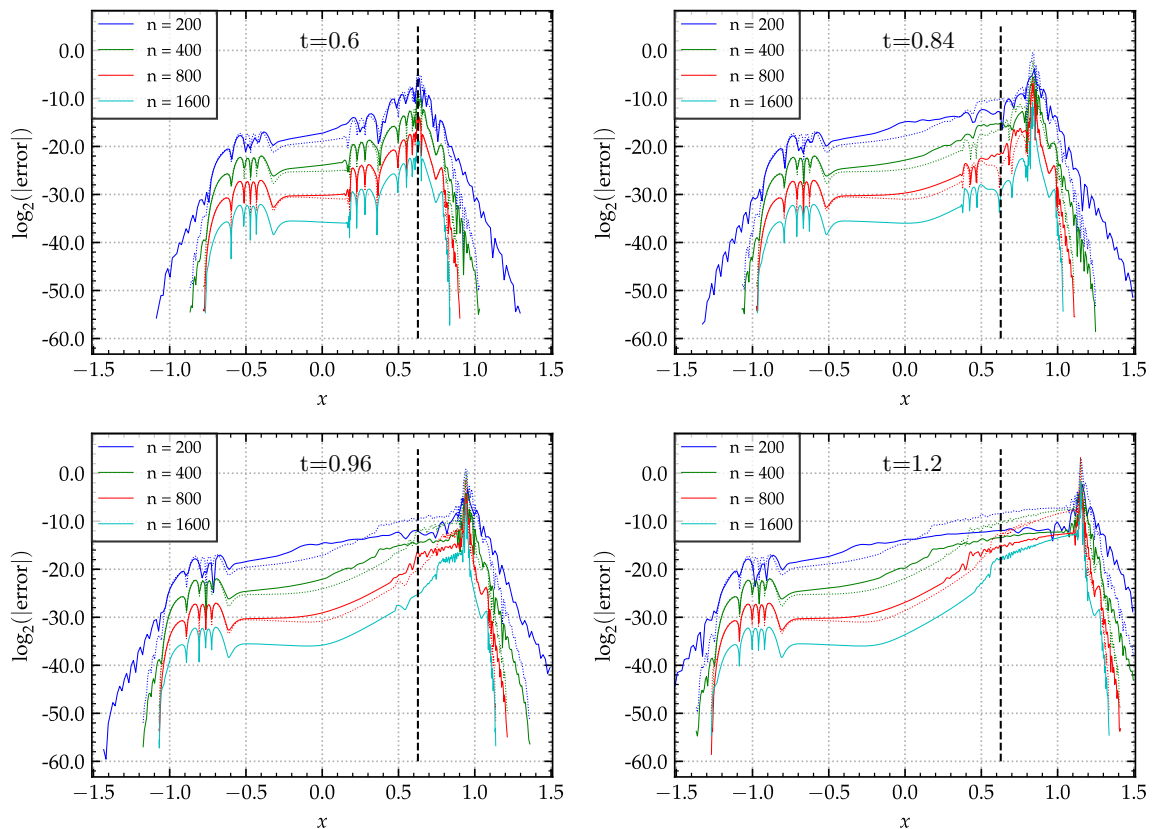


FIG. 7. Behaviour of the simple wave’s numerical error with increasing resolution at different instances of the evolution. The vertical dashed black line depicts the position at which the shock is first formed. Dotted lines show results scaled to fifth-order.

tions of special-relativistic hydrodynamics (SRHD) that demonstrate some of the main features of non-linear wave propagation, such as steepening, breaking, and shock formation. Simple wave solutions can be written analytically in an implicit form using the method of characteristics. The study of relativistic simple waves sheds light on the problem of relativistic shock formation due to non-linear steepening. Like Burgers equation the relativistic simple wave starts off from smooth initial data and at some point of its evolution develops a shock. These analytic solutions have been discussed in [35, 36]. Here, we use the simple wave described in [7], therein the initial velocity profile is of the form

$$v = a \Theta(|x| - X) \sin^6 \left(\frac{\pi}{2} \left(\frac{x}{X} - 1 \right) \right), \quad (19)$$

where $\Theta(x)$ is the Heaviside function, $a = 0.5$ and $X = 0.3$. For the construction of the initial data a polytropic EoS, $p = K\rho^\gamma$, with $K = 100$ and $\gamma = 5/3$ is employed; this data is then evolved using a Γ -law EoS (15) with $\Gamma = 5/3$. During the evolution the smooth initial profiles of all primitive variables become steeper and steeper and at around $t_{sh} \simeq 0.63$ they form a shock [35]. Numerical solutions are computed on the one-dimensional domain $x \in [-1.5, 1.5]$ with the RK4 time-integrator and a CFL factor of 0.125. The tunable constant is set to

$c_E = 10$ and the LO flux is evaluated with the WENOZ reconstruction scheme.

The top panel of FIG. 6 illustrates the evolution of the simple wave from its initial smooth configuration (19) up to the instance $t = 1.2$ when the shock has been fully formed. The solution is computed on a grid composed of 1600 points ($\Delta x = 1.875 \times 10^{-3}$). By inspection, the numerical solutions reproduce the correct physics even after the formation of the shock $t \geq t_{sh}$. No spurious oscillations are visible on the solutions, a sign that shows the effectiveness of the EFL method in suppressing oscillatory effects. The bottom panel of FIG. 6 depicts the corresponding profiles of the entropy production function ν . Clearly, the EFL method successfully locates the initial formation of the shock at $t = t_{sh}$ and effectively tracks its location at later times $t \geq t_{sh}$. During the “smooth period” $t < t_{sh}$, the entropy production is, as expected, trivial. Notice that shortly after the formation of the shock, i.e. at $t = 0.75$, the solution is oscillation-free although the contribution of the stable LO flux in the hybrid numerical flux (3) is only $\sim 33\%$. This fact points out that the EFL method can guarantee the smoothness of the solutions for some time after the shock formation without switching entirely to the LO flux. This property of the EFL method has a direct effect

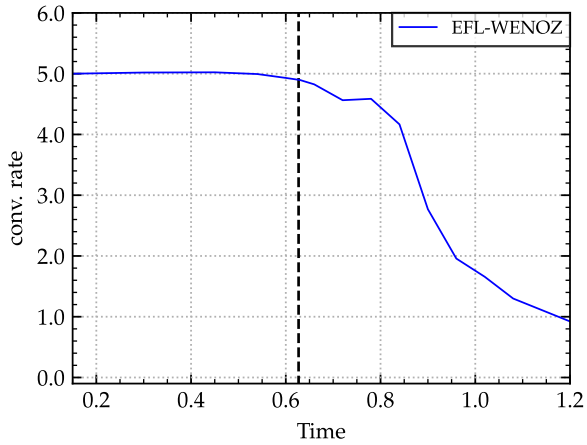


FIG. 8. Convergence rates of the simple wave with respect to the L_1 -norm. The behaviour of the convergence rates with time for the LO scheme EFL-WENOZ is shown. The vertical dashed black line depicts the instant at which the shock is first formed.

on the behaviour of the convergence rates of FIG. 8. As expected, optimal fifth-order convergence is maintained up to the formation of the shock—denoted here by a vertical dashed line. With the shock formed the convergence of our numerical solution decreases slowly up to roughly $t \sim 0.85$ —notice that the convergence rates are still higher than fourth-order. Beyond this point the convergence decreases rapidly and reaches a plateau at around 1. Clearly, there is a direct connection between the increasing use of the LO flux and the decreasing order of convergence.

FIG. 7 depicts the absolute error between the numerical and the exact solution with increasing resolution at different stages of the evolution. For times $t < t_{sh}$ before the formation of the shock the numerical error decreases to zero with the expected fifth-order convergence, see top-left panel of FIG. 7. With the formation of the shock at $t = t_{sh}$ the expected lower-order convergence spike appears. Shortly after, the numerical error converges to zero with fifth-order over the whole computational domain except at the location of the shock where the convergence drops to first-order, see top-right panel of FIG. 7. Notice that, at this stage, the convergence of the parts of the computational domain impacted by the shock is quickly restored to fifth-order. At late times, see bottom panels of FIG. 7, this is not anymore possible and the low-order convergence spreads through the computational grid at the opposite direction of the movement of the shock. This is in stark contrast with the behaviour of the numerical error of Burgers equation, see FIG. 4. The coupled non-linear nature of the SRHD equations is responsible for this difference as the EFL method operates in both cases in a similar fashion: the LO flux dominates the hybrid numerical flux (3) and its use has been restricted around the location of the shock.

B. Sod shock-tube

We move on now to a standard benchmark Riemann problem used in SRHD: the relativistic version of Sod’s shock-tube [37]. For a simple ideal fluid EoS of the form (15) with adiabatic index $\Gamma = 1.4$, the discontinuous initial data for the pressure p , the rest-mass density ρ , the velocity v , and the specific energy ϵ are the following

$$\begin{aligned} (p_L, \rho_L, v_L, \epsilon_L) &= (1, 1, 0, 2.5), \\ (p_R, \rho_R, v_R, \epsilon_R) &= (0.1, 0.125, 0, 2). \end{aligned} \quad (20)$$

The initial discontinuity at $x = 0$ splits during the evolution into a shock wave followed by a contact discontinuity, both travelling to the right, and a rarefaction wave travelling to the left. The numerical solutions are computed on the one-dimensional grid $x \in [-0.5, 0.5]$ with the RK4 scheme and a CFL factor of 0.25. The tunable constant is set to $c_E = 50$ and the WENO5 reconstruction scheme is used to evaluate the LO flux.

The top panel of FIG. 9 shows how the initial discontinuity at $x = 0$ evolves with time on a grid of 1600 points ($\Delta x = 6.25 \times 10^{-4}$). Even at early stages of the evolution the three characteristic features of Sod’s shock-tube are clearly visible: the left-moving rarefaction wave and the right-moving shock and contact discontinuities. It is evident that all the features of the Sod shock-tube are reproduced quite accurately and oscillatory effects are absent from the solutions. At the bottom panel of

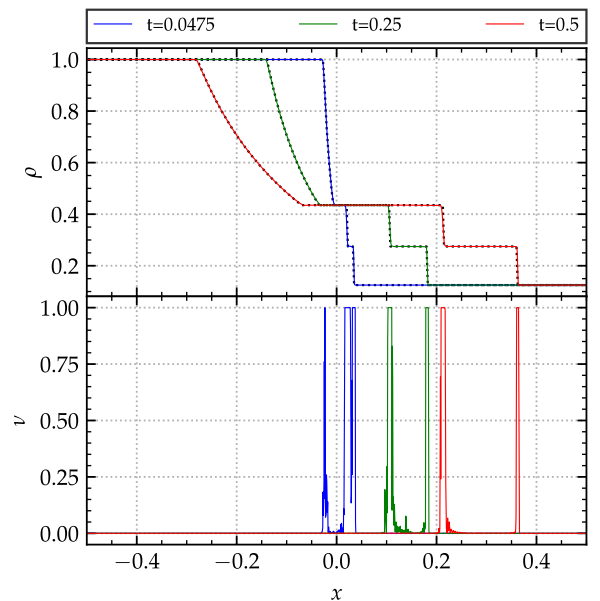


FIG. 9. Sod shock-tube. Profiles of the rest-mass density (top panel) and of the corresponding entropy production (bottom panel) at different stages of the evolution. The solution is computed with the WENO5 reconstruction scheme on a grid of 1600 points with resolution $\Delta x = 6.25 \times 10^{-4}$. Dotted black lines depict the exact solution.

FIG. 9 the corresponding entropy production profiles are shown. Again the EFL method locates and tracks the right-moving discontinuities extremely accurately. Notice that the entropy production peaks are very well localised around the position of the discontinuities, restricting in this way the use of the stable LO flux only to these problematic regions and enabling the use of the HO flux in the rest of the computational domain where the solution is smooth. At early stages of the evolutions a third entropy production peak related to the rarefaction wave is clearly visible. The initial very steep slope of the rarefaction triggers the production of this peak. With time, as the rarefaction develops, the amplitude of the entropy production peak reduces and tends to zero when the rarefaction wave has been fully developed. This comprises another manifestation of the sensitivity and accuracy of the EFL method.

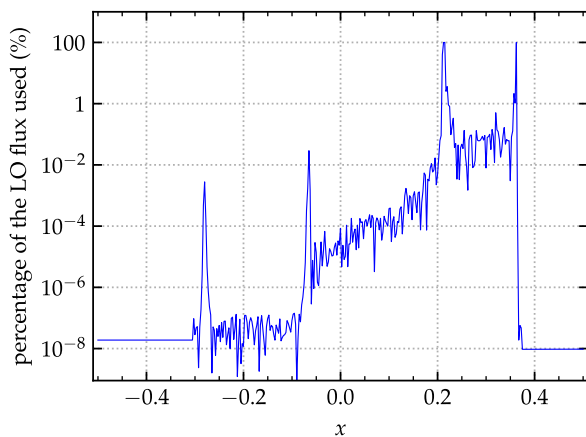


FIG. 10. Percentage of the stable LO flux used at $t = 0.5$ over the whole computational domain.

A more quantitative picture of the use of the LO flux at each point of the computational domain is given in FIG. 10. As mentioned in Sec. II the entropy production takes values in the interval $\nu \in [0, 1]$. In the extreme cases of $\nu = 0$ or $\nu = 1$ the HO or LO flux is exclusively used by the EFL method. For any other value of ν the resulting numerical flux (3) is a mix of these two fluxes. FIG. 10 shows exactly that: the percentage of each flux used at each point of the computational domain at $t = 0.5$. As expected the stable LO flux is exclusively used at the locations of the contact and shock discontinuities, in between them the use of the LO flux drops drastically to $\sim 0.5\%$ and at any other point of the computational domain does not exceed 0.01% . Notice that the positions of the head and tail of the rarefaction wave are clearly indicated by the two 0.01% entropy production peaks—the EFL method is so sensitive that recognises the slight non-smoothness of these two features compared to their neighbouring points.

Similar results we get also for the other two standard SRHD shock-tube tests: the relativistic blast wave 1 and

2 described in [38].

VI. SINGLE STAR EVOLUTIONS

We proceed further by applying the EFL method to three-dimensional general relativistic single NS spacetimes. In addition to the static TOV and rotating NS tests presented in [9], we study here a couple of more involved single NS spacetimes that unveil the ability of the EFL method to cope extremely well with non static/stationary spacetimes. The treatment of the rapidly declining gradient of the hydrodynamical variables at the surface of the NS remains also here the most challenging feature of our simulations. In addition, the non static/stationary nature of these spacetimes increases further the level of complexity we encounter. Our results are compared with those of [17, 39–41]. The EFL method is also compared to the best performing schemes currently implemented in BAM: i) a second-order scheme (LLF-WENOZ) that uses the LLF scheme for the fluxes and WENOZ for primitive reconstruction [17] and ii) a “hybrid” algorithm (HO-LLF-WENOZ) that employs the high-order HO-WENOZ scheme above a certain density threshold ρ_{hyb} and switches to the standard second-order LLF-WENOZ method below ρ_{hyb} [7].

In the following, we evolve a stable TOV star that moves along the x -direction [17, 39] and an unstable migrating NS [17, 40, 41], both in a dynamically evolved spacetime. The NS matter is here described by a Γ -law EoS with $\Gamma = 2$. The grid is composed of five fixed refinement levels. Simulations are performed at resolutions $n = (64, 96, 128)$ points leading to a grid spacing h that depends on the specific setting of the NS under investigation. For each NS configuration the resolution is explicitly given in TABLE II. It is ensured that the NS is entirely covered by the finest box at any given resolution. Radiative (absorbing) boundary conditions are used for all single star simulations.

TABLE II. Grid configurations of single star simulations. Columns (left to right): name of simulation, L : number of fixed refinement levels, n : number of points per direction, h_{L-1} : resolution per direction in the finest level $l = L - 1$, h_0 : resolution per direction in the coarsest level $l = 0$.

Name	L	n	h_{L-1}	h_0
TOV _{boost}	5	64	0.500	8.000
	5	96	0.333	5.333
	5	128	0.250	4.000
TOV _{mig}	5	64	0.125	2.000
	5	96	0.083	1.333
	5	128	0.063	1.000

A. Boosted TOV star

The Tolmann-Oppenheimer-Volkoff (TOV) initial data used here is constructed using a $\Gamma = 2$ polytrope model with $K = 100$, gravitational mass $M = 1.4$, baryonic mass $M_b = 1.506$ and central rest-mass density $\rho_c = 1.28 \times 10^{-3}$. The resulting TOV star is boosted in the x -direction at a speed of $v = 0.5$ corresponding to a Lorentz factor of $W = 1.15$. The spacetime is dynamically evolved and the BSSNOK scheme is used for the evolution of the metric.

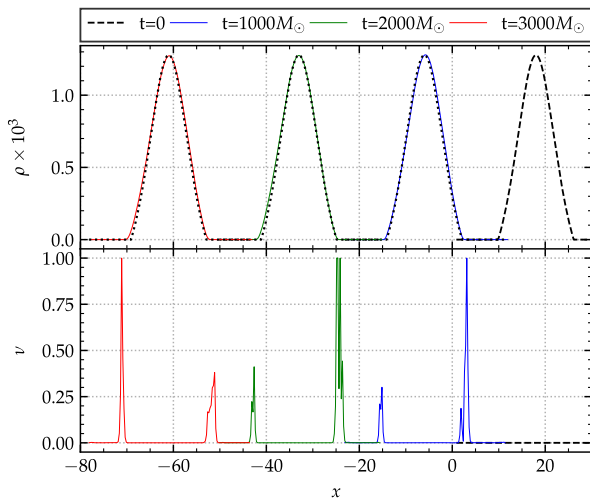


FIG. 11. Boosted TOV star. Profiles of the rest-mass density (top panel) and of the corresponding entropy production (bottom panel) at different instances of the movement of the TOV star along the x -direction. The solution is computed with the WENOZ reconstruction scheme and $n = 128$. Dotted black lines depict the exact solution.

The one-dimensional profiles of the rest-mass density (top panel) and entropy production function ν (bottom panel) are depicted in FIG. 11. The top panel shows the evolution of the TOV star along the x -direction from its initial position (dashed black lines) up to $t = 3000M_\odot$. The numerical solution reproduces quite accurately the exact one (dotted black lines) even at very late times. At the bottom panel the corresponding entropy production profiles are depicted. As expected, a local peak of the entropy production function ν is observed around the surface of the TOV star. There, the gradient of the hydrodynamical variables experiences a violent decline which leads to the production of large values of ν . In the interior of the NS the entropy production function ν is vanishing. It is evident from FIG. 11 that the EFL scheme locates and tracks extremely accurately the surface of the star during its movement along the x -axis. This, in turn, triggers the use of the stable numerical flux in the neighbourhood of the surface. The use of the stable scheme around the surface of the NS guarantees its long term stability.

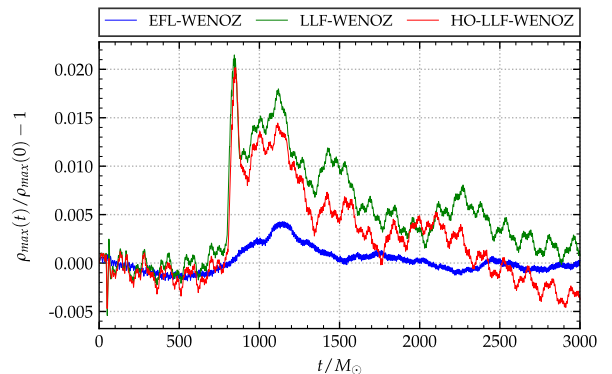


FIG. 12. Central rest-mass density evolution of a boosted TOV star in a dynamical spacetime with $n = 128$. Beside the EFL-WENOZ scheme, the LLF-WENOZ and HO-LLF-WENOZ schemes are also shown.

After securing the proper flagging of the problematic regions and the correct implementation of the EFL method, we proceed further by checking its performance during the evolution of the TOV star by monitoring the dynamical behaviour of the central rest-mass density. The oscillation of the central rest-mass density ρ_{\max} for the EFL method is presented, together with the results for the LLF-WENOZ and HO-LLF-WENOZ methods [7], in FIG. 12. Clearly, the EFL method is performing better than the LLF-WENOZ and HO-LLF-WENOZ schemes as the profile of the central rest-mass density is more stable over time and the amplitude of the oscillations is smaller.

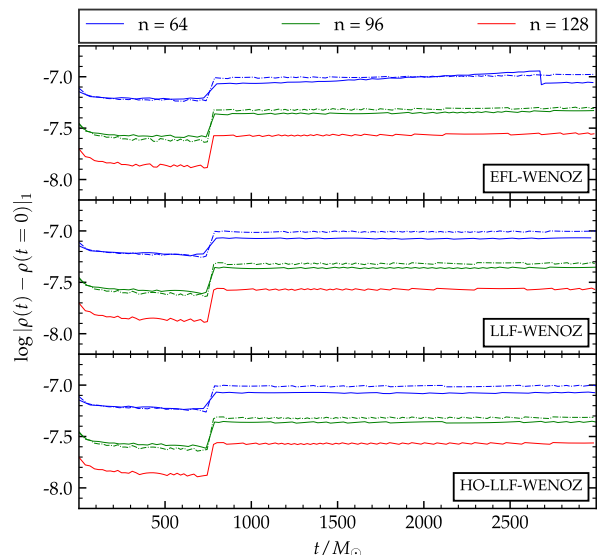


FIG. 13. Evolution of the L_1 distance $\|\rho(t) - \rho(0)\|_1$ of a boosted TOV star in a dynamically evolved spacetime. The EFL-WENOZ scheme is compared to the LLF-WENOZ and HO-LLF-WENOZ schemes. Dashed lines show results scaled to second order.

The non-dispersive character of the boosted TOV star enables us to check the convergence properties of the EFL method as the exact solution can be read off from the initial data. Here we consider the L_1 -norm of the difference between the three-dimensional evolution profile of the rest-mass density and the corresponding exact solution (initial data) and study its behaviour with time. The L_1 -distance from the exact solution for the three schemes used here are depicted in FIG. 13. The convergence rate of all the schemes considered is approximately second-order in agreement with the result of [17] and the fact that the error at the stellar surface dominates the evolution.

B. Migrating neutron star

We turn now to the study of migrating neutron stars and focus on the migration of unstable neutron stars to stable ones. This is a quite challenging test as during the process of migration oscillations of large amplitude are produced by the pulsating NS. The rapid periodic expansion and contraction of the surface of the NS is the ideal arena to test the EFL method's performance in an extreme dynamical setting where the location of the surface is constantly changing in a non-trivial way.

The unstable initial configuration we consider here is constructed using a $\Gamma = 2$ polytrope model with $K = 100$, gravitational mass $M = 1.447$, baryonic mass $M_b = 1.535$ and central rest-mass density $\rho_c = 7.993 \times 10^{-3}$ that is larger than the central rest-mass density of the stable model with the maximum possible mass. Therefore the NS is initially in an unstable equilibrium. Numerical truncation errors cause the NS to move away from this initial equilibrium and to expand, evolving gradually to smaller central rest-mass densities, until it reaches a new stable NS configuration.

The star is evolved with the Γ -law EoS and the metric components with the BSSNOK scheme. The spacetime is dynamically evolved.

We start by inspecting the one-dimensional profiles of FIG. 14 which depict the rest-mass density (top panel) and the entropy production function (bottom panel). The top panel shows the behaviour of the rest-mass density during the initial rapid expansion of the NS. The NS evolves from its initial unstable configuration at $t = 0$ to $t = 175M_\odot$ where the central rest-mass density acquires its minimum value $\rho_c = 3.139 \times 10^{-4}$, see FIG. 15. In just 0.8 ms the NS has expanded in such a degree that its central rest-mass density is about 4% of its initial value. As can be seen on the bottom panel, the EFL method reacts extremely well to this rapid change of the location of the NS surface. The peaks on the profiles of the entropy production ν are localised correctly around the moving surface of the NS ensuring that the stable numerical flux is used there. This, in turn, guarantees that the numerical solution is free of spurious oscillations and long term stable.

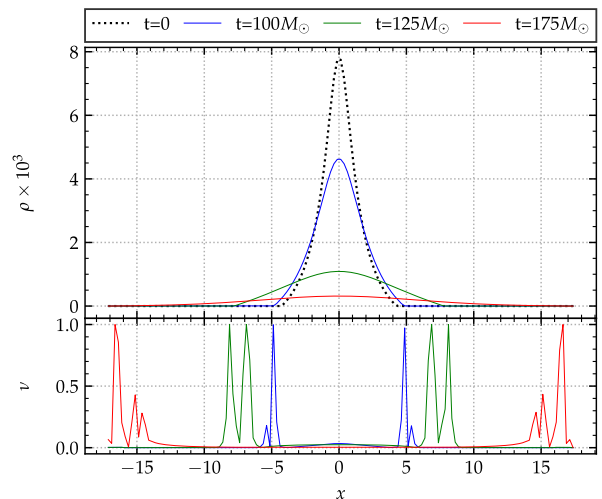


FIG. 14. Migration test. Profiles of the rest-mass density (top panel) and of the corresponding entropy production (bottom panel) at different stages of the initial rapid expansion of the migrating TOV star, see FIG. 15. The solution is computed with the WENOZ reconstruction scheme and $n = 128$.

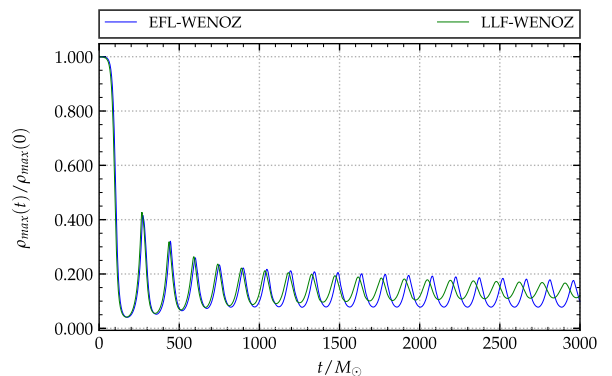


FIG. 15. Evolution of the central rest-mass density for the migration test with $n = 128$. The results of the EFL method are compared to the second-order scheme LLF-WENOZ used in [17, 24].

We continue by checking the behaviour of the central rest-mass density with time. FIG. 15 presents the evolution of the central rest-mass density for both the EFL and LLF-WENOZ method. The resulting oscillating behaviour is due to the strong non-linear pulsation of the originally unstable NS around a stable configuration. At every pulsation shock waves are formed that dissipate kinetic into thermal energy and gradually damp the oscillations. The results of the EFL method are comparable to the corresponding ones of the LLF-WENOZ scheme and the ones in [17, 40, 41].

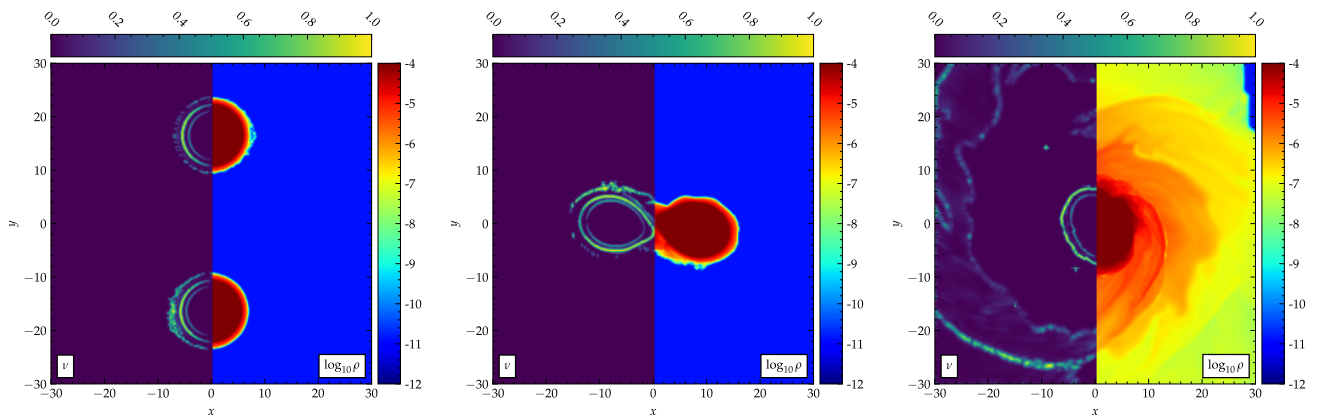


FIG. 16. Two-dimensional hybrid plots depicting the entropy production and rest-mass density profiles across different stages of the pure EFL **BAM:95** simulation. Left: inspiral. Middle: merger. Right: post-merger.

VII. BINARY NEUTRON STAR EVOLUTIONS

A. Initial data and numerical setup

We turn now to general relativistic simulations of neutron star binaries with the EFL method. In the following, we study the dynamics of a specific BNS configuration: **BAM:95** [42]. This configuration is similar to **BAM:97** [43], which was studied in the EFL framework in [9]. The main difference between these two BNS configurations lies in the way their initial data have been constructed: **BAM:97** uses the Lorene library [13] while **BAM:95** uses initial data constructed with the SGRID code [14].

We chose this BNS simulation because it enables us to study the effect of using the EFL method in the construction of the initial data. In all the BNS simulations presented in [9] the EFL method was used only in the dynamical evolution of Lorene initial data. **BAM:95** gives us the opportunity to use the EFL method in the construction of SGRID initial data through the eccentricity reduction process.

The initial data for **BAM:95** is constructed with the pseudospectral SGRID code [44–47], which makes use of the constant rotational velocity approach [14, 48] to construct spinning BNS configurations in hydrodynamical equilibrium. In accordance with [44, 49], eccentricity reduced initial data are constructed through an iterative procedure of monitoring and varying the binary’s initial radial velocity and eccentricity [44]. As an initial guess, a quasi-equilibrium configuration in the usual quasi-circular orbit is employed with residual eccentricity of the order of $e \sim 10^{-2}$. The iterative procedure consist of the following steps:

- i) Evolve the data for 2-3 orbits.
- ii) Measure the eccentricity e from the proper distance as described in [44].
- iii) Re-compute the initial data with adjusted radial velocity and eccentricity.

The actual initial data we evolve can be found in TABLE III. As mentioned above, it has been constructed with the SGRID code [14] and is characterised by the Arnowitt-Deser-Misner (ADM) mass-energy M_{ADM} , the angular momentum J_0 , the baryonic mass M_b and the dimensionless GW circular frequency $M\Omega_0$.

TABLE III. **BAM:95** initial data. Columns: name; EoS; number of orbits; binary mass; rest-mass; ADM mass; angular momentum; GW frequency.

Name	ID	EoS	orbits	M	M_b	M_{ADM}	J_0	$2M\Omega_0$
BAM:95	SGRID	SLy	10	2.700	2.989	2.678	7.686	0.038

In the present work, we chose to experiment with the use of different numerical schemes, for computing the numerical fluxes, both in the construction of the SGRID initial data and in the evolution of these data with BAM. The main reason for doing this is to study if the effect of using the EFL method will lead to higher accuracy and better convergence properties of our numerical solutions. In [42] the HO-LLF method was used both in the construction of the initial data for **BAM:95** and in its subsequent evolution with BAM. Here, we use the EFL method to conduct two additional studies of the **BAM:95** configuration. In the first, the HO-LLF method is used for the initial data construction and the EFL method for its BAM evolution. In the second, both the construction of the initial data and its BAM evolution is conducted with the EFL method. The aforementioned different combinations of numerical schemes used to study **BAM:95** in the present work are summarised in TABLE IV.

The initial data for **BAM:95** is evolved in the three different combinations of TABLE IV with the WENOZ reconstruction scheme. WENOZ reconstruction is used because the results in [9] strongly indicate that WENOZ is the best performing reconstruction scheme from those available. For each case study three different grid resolutions are considered. The grid specifications for all

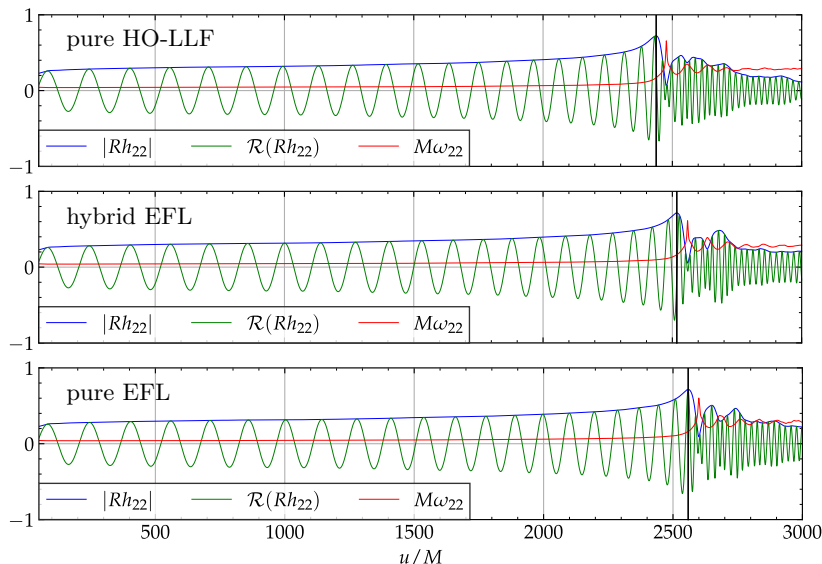


FIG. 17. **BAM:95** waveforms. The amplitude (blue line), the real part (green line) and the instantaneous frequency $M\omega_{22}$ (red line) of the GW signal obtained from the ten-orbit **BAM:95** simulation using WENOZ reconstruction for the three case studies of TABLE IV: pure HO-LLF (top), hybrid EFL (middle), and pure EFL (bottom). The time of merger is defined as the first peak of the amplitude A_{22} and is indicated by a black vertical line.

TABLE IV. **BAM:95** case studies. Columns: name of **BAM:95** case study; method used in the construction of the initial data; method used to evolve the initial data with **BAM**; reconstruction scheme used in the simulations; eccentricity.

Name	SGRID	BAM	Reconstruction	$e[10^{-3}]$
pure HO-LLF	HO-LLF	HO-LLF	WENOZ	0.4
hybrid EFL	HO-LLF	EFL	WENOZ	0.4
pure EFL	EFL	EFL	WENOZ	0.7

BAM:95 runs are the same and are reported in TABLE V. The atmosphere setting for all simulations are $f_{\text{atm}} = 10^{-11}$ and $f_{\text{thr}} = 10^2$. The metric is evolved with the Z4c scheme. Standard radiative boundary conditions are used for all BNS simulations. The behaviour and the convergence properties of the conserved quantities of the present **BAM:95** runs are similar to those of **BAM:97** presented in [9]. Therefore, in the following, for the sake of presentational brevity and clarity, we solely focus on the qualitative behaviour of the entropy production and the gravitational wave analysis of our **BAM:95** runs.

B. Qualitative behaviour of the entropy production

The entropy production function ν plays central role in our method. Hence, it is of great interest to study its behaviour during the evolution of BNS merger simulations. In the following, we discuss the two-dimensional entropy production profiles of the ten-orbit simulation **BAM:95**.

In FIG. 16 we present two-dimensional hybrid plots de-

TABLE V. Grid configurations for all the **BAM:95** case studies. Columns (left to right): name of BNS simulation; refinement levels; minimum moving level index; number of points per direction in fixed levels; number of points per direction in moving levels; resolution per direction in the finest level $l = L - 1$; resolution per direction in the coarsest level $l = 0$.

Name	L	l^{mv}	n^{fix}	n	h_{L-1}	h_0
BAM:95	7	2	160	64	0.235	15.040
	7	2	240	96	0.157	10.027
	7	2	320	128	0.118	7.520

picting the entropy production function ν and rest-mass density ρ profiles at different stages of the pure EFL simulation. (The hybrid EFL case shows similar behaviour.) The different panels show (from left to right) selected snapshots of the inspiral, merger and post-merger stages, respectively. Taking a closer look at the ν profile, we observe that during the inspiral and merger the EFL method is, as expected, only activated at the surface of each NS. The same can be also observed in the post-merger regime, however, here also regions in the exterior of the remnant NS are flagged by the EFL method. Judging from the corresponding rest-mass density plots, the observed flagging in the exterior is actually capturing the outward dynamics of the spiral density waves emitted by the rotating remnant of the two inspiraling NSs. This fact shows the effectiveness of the EFL method in locating any non-smooth features developing in the numerical domain.

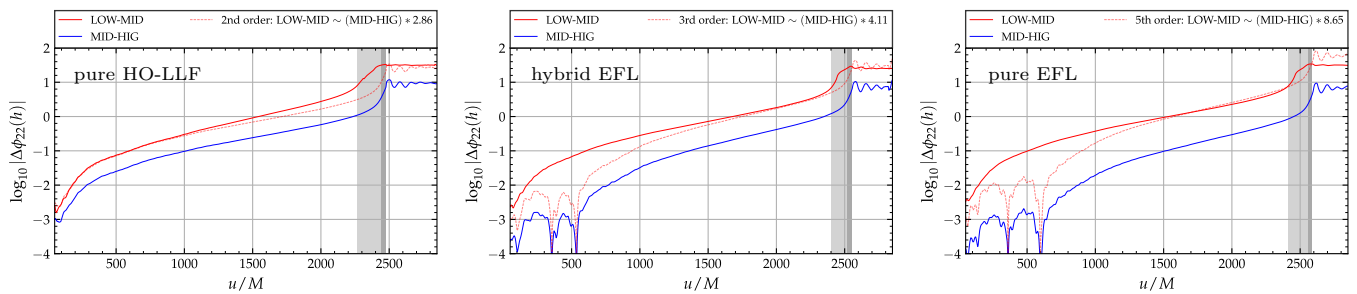


FIG. 18. GW phase difference convergence rate study for the ten-orbit BAM:95 simulation. Left: pure HO-LLF case. Middle: hybrid EFL case. Right: pure EFL case.

C. Gravitational wave analysis

We study now the effect of using the EFL method on the gravitational waveforms (GWs). Following [7, 9], we compute the GWs from the curvature scalar Ψ_4 on coordinate spheres that are at distance r from the origin of the computational domain. First, spin weighted spherical harmonics are used to expand Ψ_4 into its modes $\psi_{\ell m}$ and then the multipolar modes $h_{\ell m}$ are reconstructed by solving $\ddot{h}_{\ell m} = \psi_{\ell m}$ in the frequency domain [50]. In terms of the amplitude $A_{\ell m}$ and phase $\phi_{\ell m}$ the different modes of $h_{\ell m}$ are given by the expression

$$R h_{\ell m} = A_{\ell m} e^{-i\phi_{\ell m}}. \quad (21)$$

In the present section, we plot our results against the retarded time

$$u = t - R_* =: t - R(r) - 2M \log\left(\frac{R(r)}{2M} - 1\right), \quad (22)$$

where M is the total gravitational mass of the BNS system. $R(r) = r(1 + M/2r)^2$ is the radius in Schwarzschild coordinates and r corresponds to the radius in isotropic coordinates which is the extraction radius in our simulations. The time of merger u_{mrg} is estimated from the first peak of A_{22} of the dominant $(\ell, m) = (2, 2)$ mode

The waveforms obtained from the ten-orbit inspiral BAM:95 simulation for the three case studies of TABLE IV are presented in FIG. 17. The wave train of all three waveforms after a first peak, indicating the time of merger, shows a more complicated structure that involves multiple denser distributed peaks and a slow amplitude decay. The instantaneous GW frequency $\omega_{22} = -\mathcal{I}(\dot{h}_{22}/h_{22})$ is also plotted (red line), which undergoes a sharp frequency increase near merger (a feature characteristic of a chirp-like signal). Notice that from top to bottom the time of merger is increasing, with the difference between pure HO-LLF and pure EFL being around $u_{\text{mrg}} \approx 150M$. Clearly, the use of the EFL method elongates the inspiral and increases the merger time.

Next, self-convergence studies are performed based on simulations using $(n_i) = (64, 96, 128) \equiv (\text{LOW}, \text{MID}, \text{HIG})$ points per direction on the highest

AMR level. The phase difference between pairs of resolutions is defined by the expression

$$\Delta\phi_{\ell m}^{(n_i, n_j)} = \phi_{\ell m}^{(n_i)} - \phi_{\ell m}^{(n_j)}. \quad (23)$$

The experimental convergence rate p is determined through the rescaling of the resulting differences by a factor s that expresses the theoretically expected rate of decrease of these differences with increasing resolutions, provided of course that our simulations are converging. The definition of the factor s follows [51]:

$$s(p, n_i, n_j, n_k) = \frac{1 - (n_i/n_j)^p}{(n_i/n_j)^p - (n_i/n_k)^p}, \quad (24)$$

where $n_i < n_j < n_k$.

FIG. 18 shows a self-convergence study of the waveform phase differences for the BAM:95 simulations. The three panels (from left to right) correspond to results obtained with the pure HO-LLF, hybrid EFL, and pure EFL schemes, respectively. The pure HO-LLF result [42] (left panel) serves as a reference for comparison with the case studies involving the EFL method. Solid lines in FIG. 18 represent phase differences between runs with consecutively increasing resolutions; dashed lines correspond to rescaled differences of MID-HIG differences, where the scaling factor is computed from (24) using an integer convergence rate p ; the gray shaded regions mark the differences in merger times between runs with increasing resolution.

As expected the phase differences between runs with increasing resolutions decrease for all simulations. A feature that indicates that all schemes are capable of providing results that converge to some order. This observation is further supported by the fact that the difference between merger times is reducing, indicated by the narrowing of the gray shaded regions, with increasing resolution. Notice that, in accordance with FIG. 17, the use of the EFL method clearly increases the time of merger.

All convergence series demonstrate a clear convergence behaviour: the pure HO-LLF second-order, the hybrid EFL third-order, and the pure EFL fifth-order convergence. Comparing the results obtained with the EFL method to the ones obtained with the HO-LLF method,

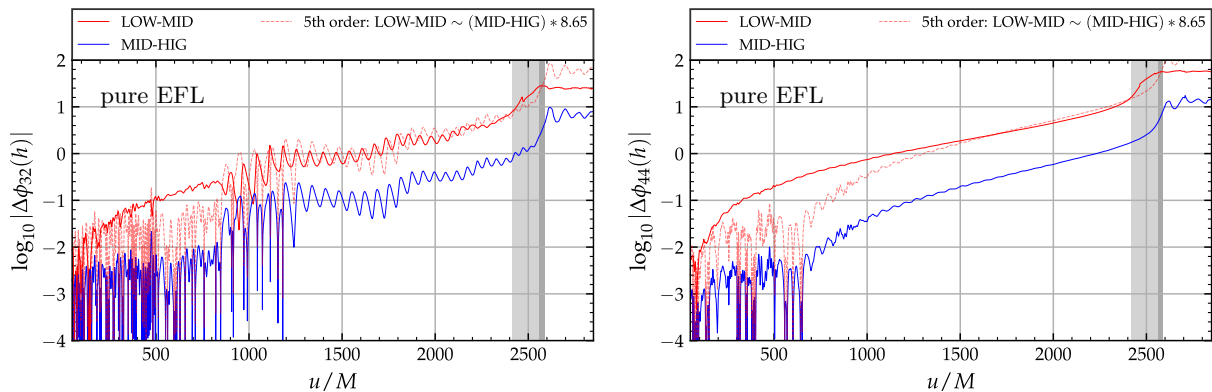


FIG. 19. GW phase difference convergence rate study for higher modes of the pure EFL ten-orbit BAM:95 simulation with WENOZ reconstruction. Left: (3, 2)-mode. Right: (4, 4)-mode.

we find that the use of the EFL method leads to higher convergence rates and to generically smaller absolute differences MID-HIG at merger. The pure HO-LLF case (left panel) yields a clear second-order convergence, consistent with the results in [42], and phase difference MID-HIG at merger a factor ~ 2 larger than the pure EFL case (right panel). We also note that in the early post-merger phase the convergence rate for the EFL cases is higher (third-order) and the difference MID-HIG smaller. An observation that unveils the robustness of the EFL method and its ability to capture satisfactorily the violent dynamics of the remnant NS.

Given this clear higher-order convergence pattern for the dominant (2, 2)-mode of the pure EFL case, it is natural to also investigate the convergence of other (subdominant) modes of $h_{\ell m}$ with $\ell > 2$. FIG. 19 shows a convergence study of the $(\ell, m) = (3, 2)$ and $(4, 4)$ modes. Also in this case, the phase differences show a consistent decrease with increasing resolution and a clear fifth-order convergence behaviour. Furthermore, a third-order convergence pattern clearly holds through merger and in the early post-merger regime.

VIII. CONCLUSIONS

The main purpose of the present work is to extend the use of the EFL method: i) to scalar PDE systems and ii) to the construction of BNS initial data sets. We address also the question whether the use of the EFL scheme in the construction of BNS initial data has a positive impact on the convergence properties of the produced gravitational waveforms. Based on our results, we answer this in the affirmative. In addition, the EFL scheme is used to successfully simulate a couple of very demanding single NS spacetimes: the migrating and boosted TOV NS.

We extend the EFL method presented in [9] and show how to generalise it to scalar PDE systems in Sec. II through the introduction of an auxiliary entropy func-

tional. The resulting EFL scheme successfully passes in Sec. IV a quite demanding set of scalar benchmark problems, with results comparable to the ones in the literature [3].

In Sec. V we revisit a couple of benchmark problems in special relativistic hydrodynamics that were also studied in [9]. Here, we focus on the study of some quantitative and qualitative properties of the entropy production function that provide a better understanding of the workings of the EFL method. Our results i) show the direct connection between the increasing use of the LO flux and the decreasing order of convergence and ii) demonstrate the extreme sensitivity of the EFL method in recognising the slightest non-smoothness features present in our solutions.

Next, the EFL method is tested in Sec. VI against three-dimensional general-relativistic non static/stationary single NS configurations. As expected, the EFL scheme accurately locates the surface of the NS, see FIG. 11 and FIG. 14, and enables the use of the LO flux in this region while the interior remains mainly resolved by the HO flux. EFL simulations give results comparable to those obtained with standard WENO schemes [17].

Finally, in Sec. VII, the entropy method is applied to a specific BNS merger simulation. The new feature that we add with the present work to the BNS simulations carried out in [9] is that the EFL method is used in the construction of the SGRID initial data through the process of eccentricity reduction. As in [9], the EFL scheme can be used to successfully evolve this initial data and the properties observed in the single star tests carry over to this simulation where the spacetime is non-stationary and the neutron stars are moving freely in the computational grid. As shown in FIG. 16, the entropy limiter locates the surface of the inspiraling NSs extremely accurately and it converges to zero in regions of smooth flows. Further, it captures the collisional shocks at merger and the outward dynamics of the spiral density waves, thus being robust also for postmerger evolutions.

A convergence study of the gravitational waveforms obtained from this simulation shows that when the EFL method is used both in the construction of the initial data and in the temporal evolution, then it can deliver fifth-order convergent waveforms at current production resolutions (Sec. VII C). Such a convergence is measured in the (2, 2) dominant mode of the strain but also in the next subdominant modes (3, 2) and (4, 4). To our knowledge, these are the first results in which fifth-order convergence is demonstrated. The estimated phase error in the waveform is about a factor ~ 2 smaller than the error in the state-of-the-art high-order WENOZ scheme used in the same BAM code, at the same resolution. Thus, we conclude that the use of the EFL scheme in the construction of the initial data can have positive impact on the accuracy and the convergence properties of BNS simulations and can be used for high-quality waveform production.

Naturally the question arises of whether the entropy pair introduced in Sec. II and used to define the entropy of systems without EoS can be also used for systems with a well defined thermodynamic entropy like the ones of Sec. V, Sec. VI and Sec. VII. Such a possibility would highly simplify the use of the EFL scheme as the same entropy pair could be used for a wide variate of different conservation laws. The investigation of this possibility is currently in progress and results will be published as soon as available.

ACKNOWLEDGMENTS

We would like to thank members of the Jena group for fruitful discussions and invaluable input. GD acknowledges funding from the European High Performance Computing Joint Undertaking (JU) and Belgium, Czech Republic, France, Germany, Greece, Italy, Norway, and Spain under grant agreement No 101093441 (SPACE) and from the EU Horizon under ERC Starting Grant, grant agreement no. BinGraSp-714626. SB acknowledges funding from the EU Horizon under ERC Starting Grant, grant agreement no. BinGraSp-714626, and ERC Consolidator Grant, grant agreement no. InspiReM-101043372. WT acknowledges support by the National Science Foundation under grant PHY-2136036.

Computations were performed on the ARA and DRACO clusters at Friedrich Schiller University Jena. The ARA cluster is partially funded by the DFG grants INST 275/334-1 FUGG and INST 275/363-1 FUGG, and ERC Starting Grant, grant agreement no. BinGraSp-714626. The authors also gratefully acknowledge the Gauss Centre for Supercomputing e.V. (www.gauss-centre.eu) for funding this project by providing computing time on the GCS Supercomputer SuperMUC-NG at Leibniz Supercomputing Centre (www.lrz.de) with the allocations pn36ge and pn36jo.

-
- [1] B. P. Abbott *et al.* (Virgo, LIGO Scientific), GW170817: Observation of Gravitational Waves from a Binary Neutron Star Inspiral, *Phys. Rev. Lett.* **119**, 161101 (2017), arXiv:1710.05832 [gr-qc].
- [2] B. P. Abbott *et al.* (GROND, SALT Group, OzGrav, DFN, INTEGRAL, Virgo, Insight-Hxmt, MAXI Team, Fermi-LAT, J-GEM, RATIR, IceCube, CAAS-TRO, LWA, ePESSTO, GRAWITA, RIMAS, SKA South Africa/MeerKAT, H.E.S.S., 1M2H Team, IKI-GW Follow-up, Fermi GBM, Pi of Sky, DWF (Deeper Wider Faster Program), Dark Energy Survey, MASTER, AstroSat Cadmium Zinc Telluride Imager Team, Swift, Pierre Auger, ASKAP, VINROUGE, JAGWAR, Chandra Team at McGill University, TTU-NRAO, GROWTH, AGILE Team, MWA, ATCA, AST3, TOROS, Pan-STARRS, NuSTAR, ATLAS Telescopes, BOOTES, CaltechNRAO, LIGO Scientific, High Time Resolution Universe Survey, Nordic Optical Telescope, Las Cumbres Observatory Group, TZAC Consortium, LOFAR, IPN, DLT40, Texas Tech University, HAWC, ANTARES, KU, Dark Energy Camera GW-EM, CALET, Euro VLBI Team, ALMA), Multi-messenger Observations of a Binary Neutron Star Merger, *Astrophys. J.* **848**, L12 (2017), arXiv:1710.05833 [astro-ph.HE].
- [3] E. F. Toro, *Riemann Solvers and Numerical Methods for Fluid Dynamics*, 2nd ed. (Springer-Verlag, 1999).
- [4] S. Bernuzzi, A. Nagar, M. Thierfelder, and B. Brügmann, Tidal effects in binary neutron star coalescence, *Phys.Rev.* **D86**, 044030 (2012), arXiv:1205.3403 [gr-qc].
- [5] D. Radice, L. Rezzolla, and F. Galeazzi, Beyond second-order convergence in simulations of binary neutron stars in full general-relativity, *Mon.Not.Roy.Astron.Soc.* **437**, L46 (2014), arXiv:1306.6052 [gr-qc].
- [6] D. Radice, L. Rezzolla, and F. Galeazzi, High-Order Fully General-Relativistic Hydrodynamics: new Approaches and Tests, *Class.Quant.Grav.* **31**, 075012 (2014), arXiv:1312.5004 [gr-qc].
- [7] S. Bernuzzi and T. Dietrich, Gravitational waveforms from binary neutron star mergers with high-order weighted-essentially-nonoscillatory schemes in numerical relativity, *Phys. Rev.* **D94**, 064062 (2016), arXiv:1604.07999 [gr-qc].
- [8] P. K. Sweby, High Resolution Schemes Using Flux Limiters for Hyperbolic Conservation Laws, *SIAM Journal on Numerical Analysis* **21**, 995 (1984).
- [9] G. Doulis, F. Atteneder, S. Bernuzzi, and B. Brügmann, Entropy-limited higher-order central scheme for neutron star merger simulations, (2022), arXiv:2202.08839 [gr-qc].
- [10] J.-L. Guermond and R. Pasquetti, Entropy-based nonlinear viscosity for fourier approximations of conservation laws, *Comptes Rendus Mathematique* **346**, 801 (2008).
- [11] J.-L. Guermond, R. Pasquetti, and B. Popov, Entropy viscosity method for nonlinear conservation laws, *Journal of Computational Physics* **230**, 4248 (2011), special issue High Order Methods for {CFD} Problems.
- [12] F. Guercilena, D. Radice, and L. Rezzolla, Entropy-limited hydrodynamics: a novel approach to relativistic hydrodynamics, *Comput. Astrophys. Cosmol.* **4**, 3 (2017), arXiv:1612.06251 [gr-qc].

- [13] E.ourgoulhon, P. Grandclement, K. Taniguchi, J.-A. Marck, and S. Bonazzola, Quasiequilibrium sequences of synchronized and irrotational binary neutron stars in general relativity: 1. Method and tests, *Phys.Rev.* **D63**, 064029 (2001), arXiv:gr-qc/0007028 [gr-qc].
- [14] W. Tichy, Constructing quasi-equilibrium initial data for binary neutron stars with arbitrary spins, *Phys. Rev. D* **86**, 064024 (2012), arXiv:1209.5336 [gr-qc].
- [15] F. Banyuls, J. A. Font, J. M. A. Ibanez, J. M. A. Marti, and J. A. Miralles, Numerical 3+1 General Relativistic Hydrodynamics: A Local Characteristic Approach, *Astrophys. J.* **476**, 221 (1997).
- [16] A. Mignone, P. Tzeferacos, and G. Bodo, High-order conservative finite difference GLM-MHD schemes for cell-centered MHD, *J.Comput.Phys.* **229**, 5896 (2010), arXiv:1001.2832 [astro-ph.HE].
- [17] M. Thierfelder, S. Bernuzzi, and B. Brügmann, Numerical relativity simulations of binary neutron stars, *Phys.Rev.* **D84**, 044012 (2011), arXiv:1104.4751 [gr-qc].
- [18] G. Jiang, Efficient Implementation of Weighted ENO Schemes, *J. Comp. Phys.* **126**, 202 (1996).
- [19] R. Borges, M. Carmona, B. Costa, and W. S. Don, An improved weighted essentially non-oscillatory scheme for hyperbolic conservation laws, *Journal of Computational Physics* **227**, 3191 (2008).
- [20] X. Liu and S. Osher, Convex eno high order multi-dimensional schemes without field by field decomposition or staggered grids, *J. Comput. Phys.* **142**, 304 (1998).
- [21] Del Zanna, L. and Bucciantini, N., An efficient shock-capturing central-type scheme for multidimensional relativistic flows - i. hydrodynamics, *Astron. Astrophys.* **390**, 1177 (2002), astro-ph/0205290.
- [22] J. S. Hesthaven, *Numerical Methods for Conservation Laws* (Society for Industrial and Applied Mathematics, Philadelphia, PA, 2018) <https://epubs.siam.org/doi/pdf/10.1137/1.9781611975109>.
- [23] B. Brügmann, J. A. Gonzalez, M. Hannam, S. Husa, U. Sperhake, *et al.*, Calibration of Moving Puncture Simulations, *Phys.Rev.* **D77**, 024027 (2008), arXiv:gr-qc/0610128 [gr-qc].
- [24] T. Dietrich, S. Bernuzzi, M. Ujevic, and B. Brügmann, Numerical relativity simulations of neutron star merger remnants using conservative mesh refinement, *Phys. Rev.* **D91**, 124041 (2015), arXiv:1504.01266 [gr-qc].
- [25] M. J. Berger and J. Olinger, Adaptive Mesh Refinement for Hyperbolic Partial Differential Equations, *J.Comput.Phys.* **53**, 484 (1984).
- [26] T. Nakamura, K. Oohara, and Y. Kojima, General Relativistic Collapse to Black Holes and Gravitational Waves from Black Holes, *Prog. Theor. Phys. Suppl.* **90**, 1 (1987).
- [27] M. Shibata and T. Nakamura, Evolution of three-dimensional gravitational waves: Harmonic slicing case, *Phys. Rev.* **D52**, 5428 (1995).
- [28] T. W. Baumgarte and S. L. Shapiro, On the numerical integration of Einstein's field equations, *Phys. Rev.* **D59**, 024007 (1999), arXiv:gr-qc/9810065.
- [29] S. Bernuzzi and D. Hilditch, Constraint violation in free evolution schemes: comparing BSSNOK with a conformal decomposition of Z4, *Phys. Rev.* **D81**, 084003 (2010), arXiv:0912.2920 [gr-qc].
- [30] D. Hilditch, S. Bernuzzi, M. Thierfelder, Z. Cao, W. Tichy, and B. Bruegmann, Compact binary evolutions with the Z4c formulation, *Phys. Rev.* **D88**, 084057 (2013), arXiv:1212.2901 [gr-qc].
- [31] F. Douchin and P. Haensel, A unified equation of state of dense matter and neutron star structure, *Astron. Astrophys.* **380**, 151 (2001), astro-ph/0111092.
- [32] J. S. Read, B. D. Lackey, B. J. Owen, and J. L. Friedman, Constraints on a phenomenologically parameterized neutron- star equation of state, *Phys. Rev.* **D79**, 124032 (2009), arXiv:0812.2163 [astro-ph].
- [33] M. Shibata, K. Taniguchi, and K. Uryu, Merger of binary neutron stars with realistic equations of state in full general relativity, *Phys. Rev.* **D71**, 084021 (2005), arXiv:gr-qc/0503119.
- [34] A. Bauswein, H.-T. Janka, and R. Oechslin, Testing Approximations of Thermal Effects in Neutron Star Merger Simulations, *Phys.Rev.* **D82**, 084043 (2010), arXiv:1006.3315 [astro-ph.SR].
- [35] E. P. T. Liang, Relativistic simple waves - Shock damping and entropy production, *Astrophys. J.* **211**, 361 (1977).
- [36] A. M. Anile, *Relativistic Fluids and Magneto-fluids*, by A. M. Anile, pp. 348. ISBN 0521304067. Cambridge, UK: Cambridge University Press, February 1990. (1990).
- [37] G. Sod, A survey of several finite difference methods for systems of nonlinear hyperbolic conservation laws, *J. Comput. Phys.* **27**, 1 (1978).
- [38] J. M. Marti and E. Müller, Numerical hydrodynamics in special relativity, *Living Rev. Rel.* **2**, 3 (1999), arXiv:astro-ph/9906333.
- [39] J. A. Font, M. A. Miller, W.-M. Suen, and M. Tobias, Three Dimensional Numerical General Relativistic Hydrodynamics I: Formulations, Methods, and Code Tests, *Phys. Rev.* **D61**, 044011 (2000), gr-qc/9811015.
- [40] J. A. Font *et al.*, Three-dimensional general relativistic hydrodynamics. II: Long-term dynamics of single relativistic stars, *Phys. Rev.* **D65**, 084024 (2002), arXiv:gr-qc/0110047.
- [41] I. Cordero-Carrion *et al.*, An improved constrained scheme for the Einstein equations: an approach to the uniqueness issue, *Phys. Rev.* **D79**, 024017 (2009), arXiv:0809.2325 [gr-qc].
- [42] T. Dietrich, S. Bernuzzi, and W. Tichy, Closed-form tidal approximants for binary neutron star gravitational waveforms constructed from high-resolution numerical relativity simulations, *Phys. Rev.* **D96**, 121501 (2017), arXiv:1706.02969 [gr-qc].
- [43] T. Dietrich, D. Radice, S. Bernuzzi, F. Zappa, A. Perego, B. Brügmann, S. V. Chaurasia, R. Dudi, W. Tichy, and M. Ujevic, CoRe database of binary neutron star merger waveforms, *Class. Quant. Grav.* **35**, 24LT01 (2018), arXiv:1806.01625 [gr-qc].
- [44] T. Dietrich, N. Moldenhauer, N. K. Johnson-McDaniel, S. Bernuzzi, C. M. Markakis, B. Brügmann, and W. Tichy, Binary Neutron Stars with Generic Spin, Eccentricity, Mass ratio, and Compactness - Quasiequilibrium Sequences and First Evolutions, *Phys. Rev.* **D92**, 124007 (2015), arXiv:1507.07100 [gr-qc].
- [45] W. Tichy, Black hole evolution with the BSSN system by pseudo-spectral methods, *Phys.Rev.* **D74**, 084005 (2006), arXiv:gr-qc/0609087 [gr-qc].
- [46] W. Tichy, A New numerical method to construct binary neutron star initial data, *Class.Quant.Grav.* **26**, 175018 (2009), arXiv:0908.0620 [gr-qc].
- [47] W. Tichy, Long term black hole evolution with the BSSN system by pseudo-spectral methods, *Phys.Rev.* **D80**, 104034 (2009), arXiv:0911.0973 [gr-qc].
- [48] W. Tichy, Initial data for binary neutron stars

- with arbitrary spins, Phys.Rev. **D84**, 024041 (2011), arXiv:1107.1440 [gr-qc].
- [49] K. Kyutoku, M. Shibata, and K. Taniguchi, Reducing orbital eccentricity in initial data of binary neutron stars, Phys. Rev. **D90**, 064006 (2014), arXiv:1405.6207 [gr-qc].
- [50] C. Reisswig and D. Pollney, Notes on the integration of numerical relativity waveforms, Class.Quant.Grav. **28**, 195015 (2011), arXiv:1006.1632 [gr-qc].
- [51] T. Baumgarte and S. Shapiro, *Numerical Relativity* (Cambridge University Press, Cambridge, 2010).